ARTICLE

Single-Crystal Intermetallic M—Sn (M = Fe, Cu, Co, Ni) Nanospheres as Negative Electrodes for Lithium-Ion Batteries

Xiao-Liang Wang,[†] Wei-Qiang Han,*[,†] Jiajun Chen,[‡] and Jason Graetz[‡]

Center for Functional Nanomaterials and Energy Sciences & Technology Department, Brookhaven National Laboratory, Upton, New York 11973

ABSTRACT $FeSn_2$, Cu_6Sn_5, $CoSn_3$, and Ni_3Sn_4 single-crystalline nanospheres with a characteristic uniform particle size of ~40 nm have been synthesized via a modified polyol process, aiming at determining and understanding their intrinsic cycling performance as negative electrode materials for lithium-ion batteries. We find that, in this morphologically controlled condition, the reversible capacities follow $FeSn_2 > Cu_6Sn_5 \approx CoSn_3 > Ni_3Sn_4$, which is not directly decided by their theoretical capacities or lithium-driven volume changes. $FeSn_2$ exhibits the best electrochemical activity among these intermetallic nanospheres and an effective solid electrolyte interface, which explains its superior cycling performance. The small particle dimension also improves cycling stability and Li^+ diffusion.

KEYWORDS: $FeSn_2$ • modified polyol process • cell performance • capacity • electrochemical activity • solid electrolyte interface

1. INTRODUCTION

Tin undergoes a reversible electrochemical alloying reaction with lithium and offers a high theoretical capacity of 993 mA h g^{-1} or 7313 mA h cm^{-3}. It is a very intriguing material and has the potential of replacing conventional graphite (372 mA h g^{-1} or 833 mA h cm^{-3}) for negative electrodes in high energy, volume efficient lithium-ion batteries (1–3). However, the electrode undergoes unfavorable structural deterioration because of the huge volume variation between tin and lithium tin alloy; thus the cycle life is fairly unsatisfactory.

Introducing a second metal element (M) to form a tin intermetallic compound is one promising solution that aims at taking advantage of Sn-based materials ultimately as high-performance electrodes (4–8). In essence, M buffers the volume change by forming a soft framework, stabilizes the integration of single intermetallic particle and enhances the electronic conductivity during cycling, and therefore improves the cell's performance regardless of whether M is electrochemically inactive (e.g., Cu_6Sn_5 (9–11), $CoSn_3$ (12), Ni_3Sn_4 (7), $FeSn_2$ (4, 13), $MnSn_2$ (14), $CeSn_3$ (15), $CrSn_2$ (16), and $LaSn_3$ (17)) or active (e.g., SbSn (18, 19), Ag_3Sn (20), and Mg_2Sn (21)).

As a matter of the aforementioned fact, noticeable research efforts have focused on identifying the intermetallic compositions necessary to achieve optimal capacity and stability. Nevertheless, the ideal composition remains elusive, because the cell performance of one intermetallic system varies prominently with the microstructure (e.g., size and shape) and synthesis methods and there is a lack of effective routes, especially on the nanoscale, to obtain a library of morphologically controllable systems. Somewhat better methods have been demonstrated to prepare a single intermetallic electrode with excellent performance (7, 22, 23) and such techniques as sputtering deposition or solid state sintering have been employed to combinatorially study thin-film or bulk systems (9, 24). Therefore, it is highly desirable to reliably control composition and morphology of Sn-based intermetallic nanostructures, and further, to systematically study how these properties affect anode performance. This supplies the possibility to find out the best intrinsic Sn-based anode material.

Here, we study the cycling behavior of single-crystal Cu_6Sn_5, Ni_3Sn_4, $FeSn_2$ and $CoSn_3$ nanospheres with similar size. These popular compositions exhibit the highest theoretical capacities in their phase diagrams (25). A polyol wet-chemistry reaction, slightly modified from the one proposed by Chou et al. (26, 27), was used. The process involved the reduction of $SnCl_2$ and metal precursors by $NaBH_4$ in tetraethylene glycol (TEG) at elevated temperature, in the presence of surface stabilizers polyvinylpyrrolidone (PVP) and poly(2-ethyl-2-oxazoline) (PEtOx). These uniform and monodispersed nanospheres appear as intermetallic M—Sn/M—Sn—O core—shell nanostructures with a single-crystalline core and amorphous shell.

2. EXPERIMENTAL METHODS

Chemicals. We used the following chemicals: $SnCl_2$ (anhydrous, 99% min, Alfa), $FeCl_3$ (anhydrous, 97%, Aldrich), $Cu(NO_3)_2 \cdot 3H_2O$ (ACS, 98.0—102.0%, Alfa), $CoCl_2 \cdot 6H_2O$ (99.9% metal basis, Alfa), $NiCl_2$ (anhydrous, 99% metal basis, Alfa),

* Corresponding author. E-mail: whan@bnl.gov.
Received for review March 14, 2010 and accepted April 30, 2010
[†] Center for Functional Nanomaterials, Brookhaven National Laboratory.
[‡] Energy Sciences & Technology Department, Brookhaven National Laboratory.
DOI: 10.1021/am100218v

Published on Web 05/05/2010

polyvinylpyrrolidone (PVP, MW = 360 000, Aldrich), and poly-(2-ethyl-2-oxazoline) (PEtOx, MW = 50 000, Alfa) as surface stabilizers; tetra-ethylene glycol (TEG, 99%, Alfa) as the solvent; and, $NaBH_4$ (98%, Alfa) as the reducing agent, and poly(vinylidene fluoride) (PVDF, Alfa).

Synthesis of Intermetallic Nanospheres. To synthesize $FeSn_2$ nanospheres, we dissolved 7.35 g of PVP (MW = 360 000) and PEtOx (3.15 g, MW = 50 000) in 157.5 mL of TEG. After heating the solution to 170 °C, a $SnCl_2$ solution (1.365 g in 14 mL of TEG) was added dropwise. After 10 min, a fresh solution of $NaBH_4$ (2.772 g in 84 mL of TEG) was added to the solution, drop by drop. The resulting solution immediately turned black, indicating the formation of Sn colloids. Sixty-five minutes later, the solution was heated to 205 °C, at which point an $FeCl_3$ solution (0.868 g in 14 mL of TEG) was added dropwise. The molar ratio n(Fe):n(Sn) was 3:4. The temperature was kept constant for 2 h. Finally, the solution was cooled to room temperature. The synthesis was carried out while vigorously stirring the solution under Ar atmosphere using a Schlenk line. The resulting nanospheres, collected by centrifugation, were washed with ethanol. The n(transition metal):n(Sn) = 3:4 and the procedures for synthesizing intermittent Sn nanoparticles were kept the same while making other systems. For the Cu_6Sn_5 nanospheres, the solution was adjusted to 150 °C before adding a $Cu(NO_3)_2 \cdot 3H_2O$ solution (1.302 g in 17.5 mL of TEG) and the temperature was then held for 40 min. For the $CoSn_3$ system, a $CoCl_2 \cdot 6H_2O$ solution (1.288 g in 14 mL of TEG) was added at 170 °C and the solution was then heated at 195 °C for 1.5 h. For the Ni_3Sn_4 system, the solution was cooled to 150 °C and then a $NiCl_2$ solution (0.7 g in 17.5 mL of TEG) was added. The temperature was held for 1.5 h before cooling down.

Characterization. The scanning electron microscopy (SEM) imaging was carried out using a Hitachi S-4800 SEM. The size distributions of the nanoparticles were obtained by measuring the particle diameters using the SEM images. We acquired the high-resolution transmission electron microscopy (HRTEM) images with a JEM-2100F TEM with a field-emission gun and an energy-dispersive X-ray spectroscopy (EDS) detector. The nanospheres were deposited on carbon-coated Cu grids in the case of $FeSn_2$, $CoSn_3$, and Ni_3Sn_4, or Ni grids in the case of Cu_6Sn_5. The powder X-ray diffraction (XRD) patterns were collected by a Rigaku/Miniflex diffractometer with Cu K_α radiation. The synchrotron XRD was carried out using beamline X7B at National Synchrotron Light Source at Brookhaven National Laboratory. The wavelength was 0.3184 Å. The electrode films for measuring cell performance consisted of intermetallic nanospheres, carbon black (Super P Li, TIMCAL), and PVDF binder with a weight composition of 64:16:20. Copper foils (0.025 mm thick, 99.8%, Alfa) served as the current collector. The electrolyte solution was 1.0 M $LiPF_6$ in ethylene carbonate/dimethyl carbonate (1:1 by volume, purchased from Novolyte). A 20 μm polyolefin microporous membrane (Celgard 2320) served as the separator. We fabricated laminated 2032-type coin cells with an electrode film/electrolyte-saturated separators/lithium foil (as the counter- and reference-electrode, 0.75 mm thick, 99.9% metal basis, Alfa) inside an M. Braun LabMaster 130 glovebox under an Ar atmosphere. The cell cycling was performed using an Arbin MSTAT system by a galvanostatic cycling procedure. The voltage range was 0.05 to 1.5 V, and the current applied was C/20 (i.e., the time for full charge or discharge of the theoretical capacity was 20 h).

3. RESULTS AND DISCUSSION

The X-ray diffraction (XRD) spectra (Figure 1) demonstrate that the nanospheres' crystal structures are $FeSn_2$ (tetragonal crystal structure, *I*4/*mcm* space group), Cu_6Sn_5 (monoclinic, *C*2/*c*), $CoSn_3$ (orthorhombic, *Cmca*) and Ni_3Sn_4 (monoclinic, *C*2/*m*), respectively. $FeSn_2$, Cu_6Sn_5, and $CoSn_3$ samples are pure phases, whereas, the Ni_3Sn_4 sample contains a small amount of a secondary phase resembling $NiSn_3$ (26). Core−shell nanostructures were characterized by transmission electron microscopy (TEM) imaging (Figure 2 and Figure S1 in the Supporting Information) and energy dispersive X-ray spectroscopy (EDS) under STEM mode using 0.7 nm probe size (Figure S2 in the Supporting Information). The particles consist of single crystalline cores covered by ~2 nm thick M−Sn−O amorphous shells.

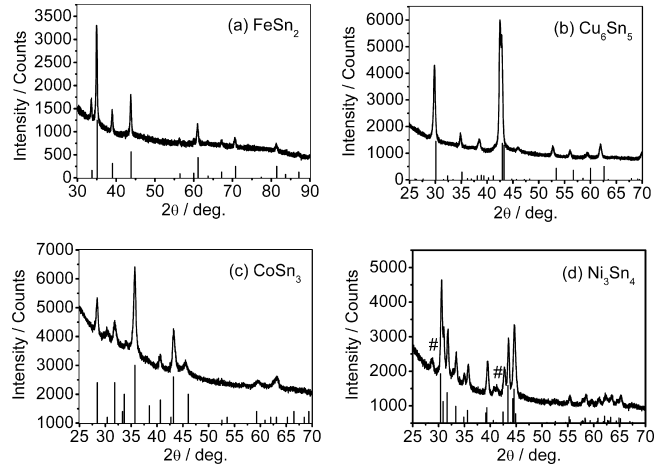

FIGURE 1. XRD patterns of (a) $FeSn_2$, (b) Cu_6Sn_5, (c) $CoSn_3$, and (d) Ni_3Sn_4 nanospheres. In d, the "#" peaks may be assigned to $NiSn_3$, as described in the text. Top, experimental; bottom, from PDF cards ($FeSn_2$, 00−025−0415; Cu_6Sn_5, 00−045−1488; $CoSn_3$, 00−048−1813; Ni_3Sn_4, 03−065−4553).

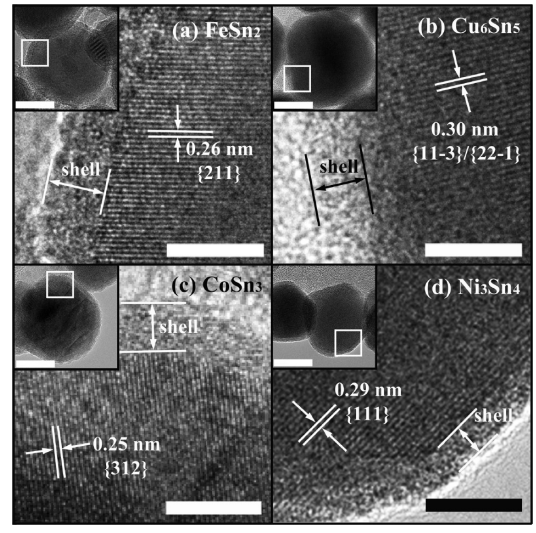

FIGURE 2. HRTEM images of (a) $FeSn_2$, (b) Cu_6Sn_5, (c) $CoSn_3$, and (d) Ni_3Sn_4 nanospheres, zoomed in from the square areas in insets. The scale bars are 5 and 20 nm (insets).

The scanning electron microscope (SEM) images in Figure 3 illustrate the predominantly spherical morphologies. As observed, the particles are fairly uniform and monodispersed. Most crucially, we are able to manipulate nanospheres of all compositions with a relatively uniform statistical size of about 40 nm.

As discussed above, we have obtained $FeSn_2$, $CoSn_3$, Cu_6Sn_5, and Ni_3Sn_4 intermetallic nanospheres with a similar morphology and nanostructure,. This will enable a better understanding of the more intrinsic difference in the cycling

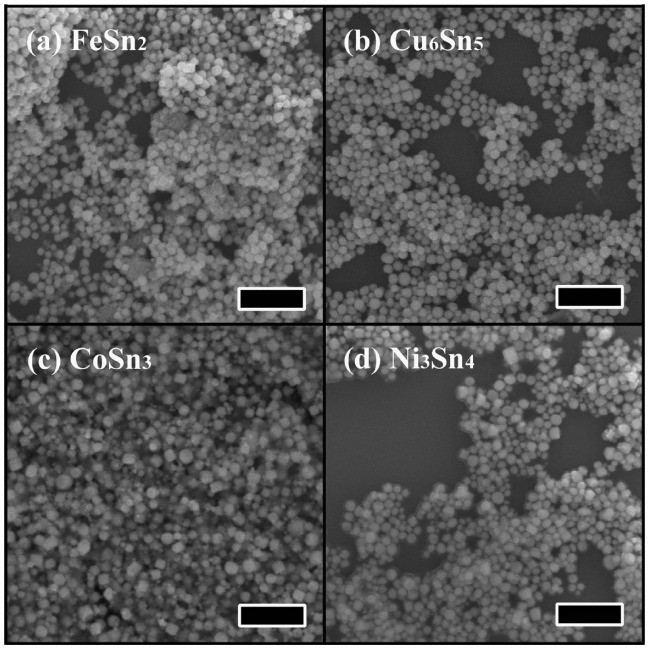

FIGURE 3. SEM images of (a) $FeSn_2$, (b) Cu_6Sn_5, (c) $CoSn_3$, and (d) Ni_3Sn_4 nanospheres. The scale bars are 300 nm.

behavior of the anode materials in Li-ion batteries, i.e., emphasizing the effects of composition and crystal structure while minimizing the influences of size and shape.

The electrochemical process of these electrodes involves a metal displacement reaction [the early redox interaction of lithium ions is inserted for Cu_6Sn_5 (9) and $CoSn_3$ (12); it involves the displacement of tin atoms, during Li^+ intake, to alloy with lithium, and simultaneously the formation of electrochemically inactive transition metal frameworks that ameliorate the impact of the volume expansion. Although the Cu_6Sn_5 and $FeSn_2$ phases could be at least partially reformed upon lithium removal (28, 29), the formation of the Ni and lithium tin alloy seems irreversible and the subsequent cycling is between lithium tin and tin metal (7). The $CoSn_3$ evolution has yet to be well determined. Mössbauer spectroscopy results support an irreversible destruction of the $CoSn_3$ phase (12, 30). However, in our preliminary synchrotron XRD observation (see Figure S3 in the Supporting Information), the initial $CoSn_3$ peaks disappeared at the end of discharge (i.e., Li^+ incorporation), and re-emerged after charging; thus, we find that this intermetallic phase exhibited some reversibility.

Figure 4 gives the reversible cell capacities for 15 cycles. $FeSn_2$ outperforms other intermetallics in its cycling performance; the reversible (Li^+ removal) capacity reaches 510 mA h g^{-1} (or 4362 mA h cm^{-3}) at the first cycle and stabilizes around 480 mA h g^{-1} upon subsequent cycling. Cu_6Sn_5 displays a higher initial capacity as compared with $CoSn_3$ but has a relatively poor cycling behavior. The capacity of Cu_6Sn_5 is exceeded by that of $CoSn_3$ after 6 cycles. In addition, Ni_3Sn_4 finishes with an inferior reversible capacity. In summary, the practical capacities of the intermetallic compounds investigated can be listed in the following order: $FeSn_2 > Cu_6Sn_5 \approx CoSn_3 > Ni_3Sn_4$. For reference, the theoretical values are $CoSn_3$ (852 mA h g^{-1}) > $FeSn_2$ (804

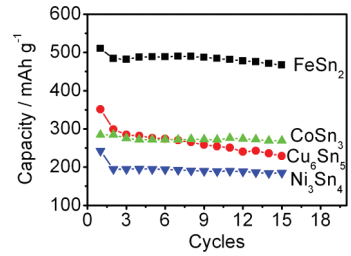

FIGURE 4. Reversible (Li^+ removal) capacities of coin cells with intermetallic nanospheres as the working electrodes and lithium metal as both the reference and counter electrodes. The cycling rate was *C*/20 based on the theoretical capacity of each system. The voltage range was 0.05−1.5 V.

mA h g^{-1}) > Ni_3Sn_4 (725 mA h g^{-1}) > Cu_6Sn_5 (605 mA h g^{-1}). Surprisingly, the volume discrepancy between the charged and discharged phases seems to have little influence on the cycling performance, because the best performance was observed with $FeSn_2$, one of the most expansive systems. If assuming the lithiated product to be $Li_{4.4}Sn$, the volume of $Li_{4.4}Sn$ is 340% that of $FeSn_2$ as compared to 308% for Ni_3Sn_4, 238% for Cu_6Sn_5, and 349% for $CoSn_3$.

The superior anode performance of $FeSn_2$ may stem from its better electrochemical activity (evidently, the initial Li^+ intake capacity exceeds the theoretical value, see Figure S4a in the Supporting Information) and the fact that $FeSn_2$ forms a favored solid electrolyte interface (SEI) layer, which could allow good cycliability without consuming much active Li^+ (as reflected by the plateau around 0.8 V in the galvanostatic discharge curve and the corresponding peak in the differential dQ/dV curve, see Figure S4 in the Supporting Information). On the contrary, the Cu_6Sn_5 system does not show a plateau at ~0.8 V in the first discharge curve suggesting it may not be protected by an effective SEI layer. This may account for its capacity loss upon cycling. The $CoSn_3$ system shows inferior electrochemical activity (lower initial discharge capacity than the theoretical value) and loses Li^+ because of SEI formation and/or other irreversible side reactions. The electrochemical performance of Ni_3Sn_4 is also characteristic of inadequate electrochemical activity. Moreover, the slight decrease in capacity of $FeSn_2$, Cu_6Sn_5, and Ni_3Sn_4 during the second cycle may imply that some SEI formation is still taking place while the robust SEI covering on the $CoSn_3$ nanoparticles ceases the irreversible reactions after the first cycle.

Structurally, the open channels located within the $FeSn_2$ crystal lattice (cf. Figure 5a and Figure S5 in Supporting Information) promote the penetration and alloying of Li^+ with the Sn host, which is responsible for the good electrochemical activity (4). Particularly, the fact that the channels parallel to [001] direction are surrounded by adjacent Sn atoms further facilitates the metal displacement reaction. Although $CoSn_3$ also possess large channels along the [001] direction, there are less-accessible Sn layers in the middle of the closely packed blocks parallel to (100) plane. Moreover, the channels in the other intermetallic systems are smaller, distorted, and/or mixed with Sn atoms and transition metal atoms (see Figure 5 and Figure S5 in the Supporting Information), which likely limit Li^+ transportation. Even

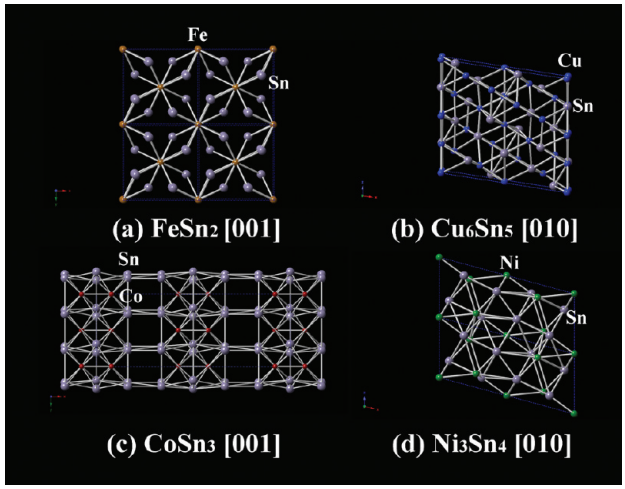

FIGURE 5. Crystal Structures of (a) $FeSn_2$, (b) Cu_6Sn_5, (c) $CoSn_3$, and (d) Ni_3Sn_4 from representative view directions.

in the circumstance that there are no accessible channels, Li^+ mainly reacts with Sn atoms at the particle/grain surfaces; thus the extruded transition metal atoms could form an impenetrable "skin" that shields the inner Sn source from alloying (4).

The first electrochemical studies of $FeSn_2$ (prepared by high-temperature melting, ~600 mA h g^{-1} initially and ~100 mA h g^{-1} after 15 cycles) showed capacity reduction upon cycling (4). Therefore, the improved cyclability of $FeSn_2$ nanospheres in the present work suggests that the reduced particle dimensions are responsible for the stability and reactivity. The smaller particles tend to have less absolute volume change upon cycling and enable effective Li^+ conduction as a result of shortened diffusion distance.

4. CONCLUSIONS

We prepared ~40 nm single-crystalline $FeSn_2$, Cu_6Sn_5, $CoSn_3$ and Ni_3Sn_4 nanospheres by a modified polyol process, using $NaBH_4$ as the reducing agent. The MSn_x cores were covered with ~2 nm oxidized shells, as confirmed by TEM and STEM-EDS measurements. $FeSn_2$ nanospheres show the highest capacity of about 500 mAh g^{-1} and the capacities have the following order: $FeSn_2 > Cu_6Sn_5 \approx CoSn_3 > Ni_3Sn_4$. The stability of Cu_6Sn_5 upon cycling is relatively inferior. Good electrochemical activity observed in $FeSn_2$ is attributed to open channels in the structure (especially the ones adjacent to Sn atoms) and an effective SEI layer is responsible for the superior cycling performance. Furthermore, the small particle size is beneficial to cycling stability and Li^+ diffusion. The present work suggests that $FeSn_2$ could be one of the intrinsically high performance intermetallic anode materials for Li-ion batteries.

Acknowledgment. This work is supported by the U.S. DOE under contract DE-AC02-98CH10886 and E-LDRD Fund of Brookhaven National Laboratory. We thank Jian Hong, Feng Wang, Lihua Zhang, and Lijun Wu for their technical help and valuable discussions.

Supporting Information Available: STEM-EDS of nanospheres, synchrotron XRD, charge/discharge curves, and crystal structure in other directions (PDF). This material is available free of charge via the Internet at http://pubs.acs.org.

REFERENCES AND NOTES

(1) Winter, M.; Besenhard, J. O. *Electrochim. Acta* **1999**, *45*, 31–50.
(2) Derrien, G.; Hassoun, J.; Panero, S.; Scrosati, B. *Adv. Mater.* **2007**, *19*, 2336–2340.
(3) Obrovac, M. N.; Christensen, L.; Le, D. B.; Dahn, J. R. *J. Electrochem. Soc.* **2007**, *154*, A849–A855.
(4) Mao, O.; Dahn, J. R. *J. Electrochem. Soc.* **1999**, *146*, 414–422.
(5) Kepler, K. D.; Vaughey, J. T.; Thackeray, M. M. *Electrochem. Solid-State Lett.* **1999**, *2*, 307–309.
(6) Tarascon, J. M.; Armand, M. *Nature* **2001**, *414*, 359–367.
(7) Hassoun, J.; Panero, S.; Simon, P.; Taberna, P. L.; Scrosati, B. *Adv. Mater.* **2007**, *19*, 1632–1635.
(8) Fan, Q.; Chupas, P. J.; Whittingham, M. S. *Electrochem. Solid-State Lett.* **2007**, *10*, A274–A278.
(9) Vaughey, J. T.; Owejan, J.; Thackeray, M. M. *Electrochem. Solid-State Lett.* **2007**, *10*, A220–A224.
(10) Shin, H. C.; Liu, M. L. *Adv. Funct. Mater.* **2005**, *15*, 582–586.
(11) Finke, A.; Poizot, P.; Guery, C.; Tarascon, J. M. *J. Electrochem. Soc.* **2005**, *152*, A2364–A2368.
(12) Alcantara, R.; Nwokeke, U.; Rodriguez, I.; Tirado, J. L. *Electrochem. Solid-State Lett.* **2008**, *11*, A209–A213.
(13) Zhang, C. Q.; Tu, J. P.; Huang, X. H.; Yuan, Y. F.; Wang, S. F.; Mao, F. *J. Alloys Compd.* **2008**, *457*, 81–85.
(14) Beaulieu, L. Y.; Dahn, J. R. *J. Electrochem. Soc.* **2000**, *147*, 3237–3241.
(15) Sakaguchi, H.; Honda, H.; Akasaka, Y.; Esaka, T. *J. Power Sources* **2003**, *119*, 50–55.
(16) Xue, M. Z.; Fu, Z. W. *Solid State Ionics* **2006**, *177*, 1501–1507.
(17) Vaughey, J. T.; Thackeray, M. M.; Shin, D.; Wolverton, C. *J. Electrochem. Soc.* **2009**, *156*, A536–A540.
(18) Li, H.; Shi, L. H.; Lu, W.; Huang, X. J.; Chen, L. Q. *J. Electrochem. Soc.* **2001**, *148*, A915–A922.
(19) Wang, Y.; Lee, J. Y. *Angew. Chem., Int. Ed.* **2006**, *45*, 7039–7042.
(20) Wang, X. Y.; Wen, Z. Y.; Lin, B.; Lin, J.; Wu, X. W.; Xu, X. G. *J. Power Sources* **2008**, *184*, 508–512.
(21) Larcher, D.; Prakash, A. S.; Saint, J.; Morcrette, M.; Tarascon, J. M. *Chem. Mater.* **2004**, *16*, 5502–5511.
(22) Fan, X. Y.; Ke, F. S.; Wei, G. Z.; Huang, L.; Sun, S. G. *Electrochem. Solid-State Lett.* **2008**, *11*, A195–A197.
(23) Park, C. M.; Sohn, H. J. *Adv. Mater.* **2010**, *22*, 47–52.
(24) Todd, A. D. W.; Mar, R. E.; Dahn, J. R. *J. Electrochem. Soc.* **2006**, *153*, A1998–A2005.
(25) Okamoto, H. *Desk Handbook: Phase Diagrams for Binary Alloys*; ASM International: Materials Park, OH, 2000.
(26) Chou, N. H.; Schaak, R. E. *J. Am. Chem. Soc.* **2007**, *129*, 7339–7345.
(27) Chou, N. H.; Schaak, R. E. *Chem. Mater.* **2008**, *20*, 2081–2085.
(28) Larcher, D.; Beaulieu, L. Y.; MacNeil, D. D.; Dahn, J. R. *J. Electrochem. Soc.* **2000**, *147*, 1658–1662.
(29) Mao, O.; Dunlap, R. A.; Dahn, J. R. *J. Electrochem. Soc.* **1999**, *146*, 405–413.
(30) Ortiz, G. F.; Alcantara, R.; Rodriguez, I.; Tirado, J. L. *J. Electroanal. Chem.* **2007**, *605*, 98–108.

AM100218V